First-principles simulation of intense single-cycle ultrashort light pulses interacting with diamond: Comparison study in attosecond and femtosecond regimes

Xiurong Feng,[1] Feng Wang [ORCID],[1,*] Suna Pang,[1] Zehui Liu,[1] Xiaowei Sheng,[2] and Jian Wang [ORCID][3]

[1]*School of Physics, Beijing Institute of Technology, Beijing 100081, China*
[2]*Department of Physics, Anhui Normal University, Anhui, Wuhu 241000, China*
[3]*School of Science, Huzhou University, Zhejiang 100083, China*

The interaction of intense single-cycle ultrashort (0.1 to 9 fs) light pulses with diamond crystal and thin film is simulated, combining the dependent Kohn-Sham equation with the Maxwell equations. Distinct features are observed depending on the duration of the pulse. In the diamond crystal, maximum energy transfer from light pulse is observed with a pulse duration 0.3 fs. In this case, the phase of current density $J(t)$ coincides with that of the electric field $E(t)$. For the incident pulse of duration 0.1 fs, most of the light will transmit on passing the thin film. But for the pulse of duration 0.5 fs, there is more reflection than transmission. For light pulses of durations 7 and 9 fs in diamond crystal, traditional nonlinear behavior of energy transfer are observed. Interestingly, for the attosecond pulse, there is a linear scaling behavior with the pulse intensity below 10^{16} W/cm^2 on the one hand and an unusual linear dynamic interference response behavior with the pulse width, determined by the interference of the different quantum pathways, on the other hand.

I. INTRODUCTION

Several advances in the generation of attosecond light pulses [1–13] have been made in the past two decades. For example, the duration of the attosecond laser pulse has been shortened to 43 as [11], the intensity of available isolated attosecond laser pulse could reach the order of 100 TW [13], and the intensity of a train of attosecond pulses is about 10^{15} W/cm^2 [14].

The unusual capability of the attosecond technology lies in probing, initiating, driving, and controlling ultrafast electronic dynamics in atoms, molecules, and solids with unprecedented high temporal and spatial resolutions simultaneously. The examples are observing the valence electron movement of krypton ions [15], the alternating Stark effect of excited electrons in helium atoms [16], and the autoionization of argon atoms [17] by using attosecond transient absorption spectroscopy, the measurement of temporal delays in the photoemission of electrons from different atomic orbitals of argon on the attosecond timescale [18], tunneling delay time measurements using attosecond angular streaking in helium [19], tracking rearrangement of the electronic system of a core-excited krypton atom with attosecond resolution [20], observation of the relative photoemission timing of helium photoelectrons with subattosecond precision [21], attosecond control of ionization by wave-packet interference of helium and argon [16], attosecond real-time observation of electron tunneling in neon and xenon atoms [22] in atomic systems; reconstruction of excited state time-dependent wave function in H_2 molecules [23], measurement of the lifetime of the autoionization Rydberg state [24], and the dynamics of Ryd-

berg and valence states in N_2 molecules [25] with attosecond transient absorption spectroscopy, prompting ionization and detecting ultrafast dynamics of the amino acid phenylalanine by attosecond pulses [26], the control of the dissociation pathway in a hydrogen molecular ion by using a pair of attosecond pulse trains [27], the electron localization of hydrogen molecules (H_2, D_2) on attosecond timescales [28], attosecond imaging of electronic wave packet of H_2 molecules with angstrom resolutions [29] in molecular systems; attosecond near-field retrieval with a gold nanotip using streaking spectroscopy [30], attosecond control of electrons photoemission from a nanoscale tungsten tip [31], observation of dielectric shielding and electron propagation from Mg/W on the atomic length scale in attosecond spectroscopy [32], attosecond control of the ultrafast field-induced insulator-to-conductor state transition in SiO_2 dielectric from attosecond streaking [33], and investigation of the GaAs subfemtosecond response induced by resonant intense near-infrared laser pulses using attosecond transient absorption spectroscopy [34] in solid systems.

It should be noted that shaping laser beams, e.g., tailoring the spatial transversal intensity distribution by static or dynamic beam shapers, shaping the intensity distribution in propagation direction by axicons or modifying the temporal shape and phase fronts, have already been demonstrated in laser micromaterial processing [35], such as semiconductor chip fabrication. Optimal control of electronic states in material with the help of suitably shaped temporal pulse envelopes offers the extended flexibility to guide the material response towards user-designed directions, giving a possibility for quality material processing [36]. Obviously the ability to shape attosecond light pulses in both temporal and spatial domains has been the foundation of attosecond science and technology. However, attosecond light pulses cannot be easily shaped

*wangfeng01@tsinghua.org.cn

temporally or spatially into the specifically designed wave forms by conventional approaches of pulse shaping due to its broadband spectra covering the energetic extreme ultraviolet to the x-ray range, compared with longer light pulses. Indeed, the wave form of attosecond light pulses can be shaped by several approaches, such as using a thin aluminum filter [37], semiconductor (Si) and metallic (Al, Zr) transmission filters [38], a broadband Cr/Sc multilayer mirror [39], an aperiodic $B_4C/Mo/Si$ multilayer mirror [40,41], a periodic Si/Sc multilayer mirror [42], seeded free-electron laser [43] partial phase matching [44], and manipulating the driving field [45].

On account of the ultrashort duration of attosecond light pulses, its interaction with matter is distinguished from conventional long light pulses by a combination of the following features. (i) One and the same electron state in matter encounters all photons contained in an attosecond light pulse at the same time, enabling therefore interferences between pathways involving different intermediate states that are sensitive to the phase between these photons. (ii) A wide spectral band of photons contained in an attosecond light pulse offers new possibilities to have interferences between more quantum channels, promising a much higher degree of attainable control of electron states in matter. (iii) For high energetic photons contained in an attosecond light pulse, deeper electron states in matter become accessible, electron correlation and multielectron dynamics become increasingly important, leading to the excitation of multiple electrons with a single photon. (iv) Attosecond light pulse provides a direct method to explore and control the microscopic motion of electrons in speed matched to the electronic timescale. Here, of particular interest, is for us to explore the characteristic features of shaping intense attosecond light pulses with matter films, in contrast to the intense femtosecond light pulses. Hence, a fundamental question is how does an attosecond light pulse interact with and propagate through matter films. While on the one hand this type of research is important from a fundamental point of view as it can provide important insights into the complex interaction between attosecond light pulse and matter in previously unexplored regimes of parameters where electron correlation, collective effects, matter characteristics, phase between photons contained in an attosecond light pulse, and film geometries becomes increasingly important; on the other hand, this research also comprises considerable potential for applications in designing devices for shaping attosecond light pulses.

In this paper the interplay between a series of specifically designed intense single-cycle attosecond light pulses and diamond thin films of various thicknesses from a few atomic layers to a few tens of nanometers is investigated to explore the unique capability of shaping attosecond light pulses. Our calculation is based on a coupled first-principles approach [46,47] in which both dynamics of electron motion and light propagation are treated consistently in a multiscale procedure, since the full description of an interplay between attosecond light pulses and matter films requires inclusion of propagation through the film medium, phase matching effects, reflection, transmission, and absorption. In order to obtain a complete understanding of propagation effects, we conduct a comparison study in attosecond and femtosecond regimes.

The organization of the paper is as follows. Section II describes in brief the theoretical framework and the simulation details. The calculated results and discussion are presented in Sec. III. Finally, the conclusion of the paper is given in Sec. IV.

II. THEORETICAL FRAMEWORK

From the theoretical point of view, the light-matter interaction is intrinsically a complex process involving dynamics of electrons, ions, and electromagnetic fields, which couple each other in different scales of space and time. In physics there are different theoretical approaches in explaining various light-matter interaction phenomena with various spatial and temporal resolutions under various approximations. Among the various approaches, the first-principles computational approaches based on density-functional theory (DFT) have been widely used to describe the interaction of light with bulk materials. There are two basic approaches, one is solved in frequency domain to gain insight into the linear optical response of matter to an external weak light field, and the other is in time domain. The advantage of the latter is that it can also be applied to nonlinear light-matter interaction under an intense light field. Generally speaking, the interaction of ultrashort light pulses with bulk materials can take place in various forms depending on various parameters characterizing the bulk materials and the wave form of light pulses. Correspondingly, there are different levels of approaches, under different approximate conditions applicable to the study of the interaction of intense laser light with bulk materials at different spatial and temporal scales. For instance, in the case of pulses shorter than the characteristic timescale of energy transfer from the electrons to the ions, it is safe to say that such pulses excite only electrons during the light-matter interaction, leaving the atomic structure intact. There is a ladder of approximations for the first-principles computational approaches in time domain. At the lowest rung of this ladder, in order to describe the electron dynamics in bulk materials under light fields, the time-dependent Kohn-Sham (TDKS) equation, which is the basic equation of time-dependent density-functional theory (TDDFT), has been solved in the time domain [48]. Higher rungs incorporate increasingly complex ingredients arising from coupled nonlinear dynamics of light electromagnetic fields and ions. Each rung incorporates the design elements of the lower rungs, and more. For instance, at the second rung, a propagation of strong light electromagnetic fields in bulk media has been incorporated, combining the Maxwell equations using multiscale computational strategy [46]. Furthermore, at the third rung, the ion or lattice dynamics have been incorporated, combining a first-principles Ehrenfest molecular dynamics (MD) approach [47]. In a practical application, the rung of this ladder can be chosen to match accuracy requirements and computational resources.

The calculation of this paper is extended to the second rung in which the propagation of the laser pulse in bulk solids is included in the simulation via coupling the electron dynamics in many microscopic unit cells with the time evolution of the electromagnetic fields in a multiscale framework. At microscopic scale, the electron motion in a unit cell of crystalline

solid is described by the TDKS equation. At macroscopic scale, the propagation of macroscopic light electromagnetic fields is described by the Maxwell equations. Besides, we consider an irradiation of diamond thin films by a linearly polarized few cycle attosecond laser pulse at normal incidence for the propagation.

It is important to note that our aim here is to investigate the effects of propagation on more delicate structures such as thin films of various thicknesses from a few atomic layers to a few tens of nanometers. Our simulations are basically carried out with SALMON code (version 1.2.1) [49,50], which is a scientific program package specially designed to study light-matter interaction problems using multiscale computational strategy. Detail of the strategy is described in Refs. [46,50,51]. We briefly summarize it below.

In SALMON, the macroscopic coordinate $\mathbf{X}$ and the microscopic coordinate $\mathbf{r}$ are introduced, respectively. First, in the microscopic scale of the unit cell, an approximation of a coarse graining is applied by treating the macroscopic field as uniform, otherwise only a longitudinal part of the vector potential is retained [52]. Under the above approximation, the propagation of macroscopic electromagnetic fields is described in the macroscopic coordinate $\mathbf{X}$ by the following Maxwell equation:

$$\frac{\partial^2 \mathbf{A}_X(t)}{\partial X^2} - \frac{1}{c^2}\frac{\partial^2 \mathbf{A}_X(t)}{\partial t^2} = -\frac{4\pi}{c}\mathbf{J}_X(t), \qquad (1)$$

where $\mathbf{A}_X(t)$ is the macroscopic vector potential and $\mathbf{J}_X(t)$ is the macroscopic electric current density, which are respectively used as input and output of the microscopic scale calculation. Note that, in principle, the electromagnetic fields could be identically described by using scalar and vector potentials in various gauges. Here, for simplicity of computations, it is convenient to adopt the so-called Weyl gauge in which the scalar potential is set to zero [52]. By the way, in the lowest level of the model, we describe electron dynamics in a unit cell of a crystalline solid with the periodic boundary conditions under a time-dependent, spatially uniform vector potential which is related to the external electric field $\mathbf{E}(t)$ by $\mathbf{E}(t) = -(1/c)d\mathbf{A}(t)/dt$. Next, the microscopic electron dynamics are described at each macroscopic grid point of $\mathbf{X}$ using the following TDKS equation:

$$\mathbf{i}\hbar\frac{\partial}{\partial t}\psi_{i,X}(\mathbf{r},t) = \hat{H}_{\mathrm{KS}}(\mathbf{r},t)\psi_{i,X}(\mathbf{r},t), \qquad (2)$$

where $\psi_{i,X}(\mathbf{r},t)$ is a Kohn-Sham one-electron orbital at point X, which distinguishes spin, and $\hat{H}_{\mathrm{KS}}$ is the time-dependent Kohn-Sham Hamiltonian defined by

$$\hat{H}_{\mathrm{KS}}(\mathbf{r},t) = \frac{1}{2m}\left(-\mathbf{i}\hbar\nabla + \frac{e}{c}\mathbf{A}_X(t)\right)^2 + V_{\mathrm{H},X} + V_{\mathrm{ion},X} + V_{\mathrm{xc},X}, \qquad (3)$$

where $V_{\mathrm{ion},X}$ is the norm-conserving pseudopotentials to deal with the interaction between valence electrons and the ionic core, $V_{\mathrm{H},X}$ and $V_{\mathrm{xc},X}$ are the Hartree potential and exchange-correlation potential, respectively. The macroscopic electric current density $\mathbf{J}_X(t)$ of Eq. (1) is an essential quantity that connects two spatial scales, defined as $\mathbf{J}_X(t) = 1/\Omega\sum_i\int_\Omega d\mathbf{r}\psi_{i,X}^*(\mathbf{r},t)\hat{\mathbf{j}}\psi_{i,X}(\mathbf{r},t)$, where Ω is the volume of the unit cell and $\hat{\mathbf{j}}$ is the electron current density
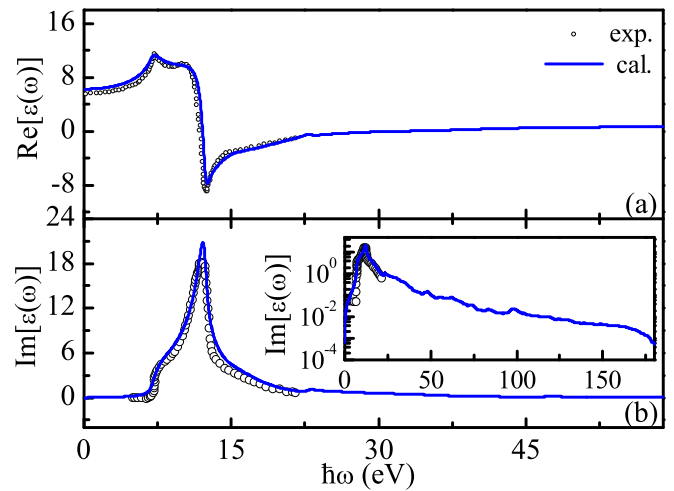

FIG. 1. The calculated real (a) and imaginary parts (b) of dielectric function $\varepsilon(\omega)$ of diamond as a function of frequency in the ground state. The illustration of the bottom panel is the logarithmic function diagram of the imaginary part of $\varepsilon(\omega)$. The dark gray circle denotes the corresponding experimental data [55,56].

operator [53,54],

$$\hat{\mathbf{j}} = \frac{1}{\mathbf{i}\hbar}[\hat{\mathbf{r}}, \hat{H}_{\mathrm{KS}}]. \qquad (4)$$

III. RESULTS AND DISCUSSION

In our numerical simulation, diamond is taken as the material to study light-matter interaction. The periodicity of diamond crystal is simulated by using a cubic cell with a lattice parameter of $a = 6.74$ a.u. The cubic unit cell contains eight carbon atoms. The first Brillouin zone in the inverted space is discretized with $8 \times 8 \times 8$ k points. And the TDKS equation is solved in a discretized three-dimensional space mesh, which is discretized into $16 \times 16 \times 16$ grid points with a grid spacing of 0.42 a.u. (atomic units used unless stated otherwise). We use the generalized gradient approximation (GGA) based on the Perdew-Burke-Ernzerhof functional (PBE). To ensure the calculation accuracy and save the calculation amount, for $T_{\mathrm{as}} = 0.1$ fs, the real-time propagation is performed with a time step of 0.005 a.u., the other attosecond propagation time step is 0.01 a.u. and the femtosecond propagation time step is 0.02 a.u.. Moreover, in the calculation of spatial propagation on the macroscale, in order to ensure the calculation accuracy, we set the macrogrid spacing as 6.74 a.u. which is the lattice parameter. Taking the attosecond light pulse as an example, it is worth noting that for the computational cost of the spatial propagation of a thin film with a thickness of $d = 29.988$ nm, it takes about 3 days on a computer system with 28 cores.

A. Energy transfer to diamond crystal

The dielectric function provides valuable information about the electronic structure and produces a complete image of the linear optical response. Therefore, first, the dielectric function of diamond is given in the ground state, as shown in Fig. 1. The illustration of the bottom panel is the logarith-

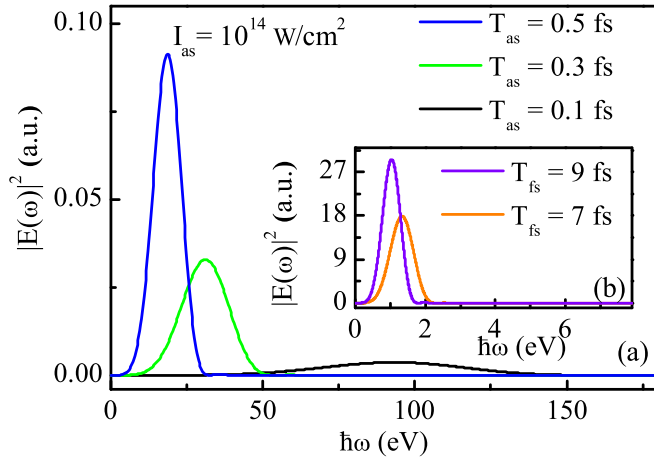FIG. 2. The photon number density distribution with the single-cycle pulse intensity of $I_{as} = 10^{14}$ W/cm^2. The panel corresponds to attosecond pulses with durations $T_{as} = 0.1$ fs, $T_{as} = 0.3$ fs, and $T_{as} = 0.5$ fs. The illustration corresponds to femtosecond pulses with $T_{fs} = 7$ fs and $T_{fs} = 9$ fs.

mic function diagram of the imaginary part of $\varepsilon(\omega)$ a wide frequency range. Obviously the real part and imaginary part of $\varepsilon(\omega)$ are in reasonable agreement with the measured data [55,56], and the imaginary part has a main absorption peak at about 12.1 eV.

Next, in the lowest level of the model, we simulate the interaction of diamond crystal with intense single-cycle ultrashort light pulses. The pulse shape is expressed by

$$A(t) = -\frac{E_0}{\omega} \cos^2\left[\frac{\pi}{T}\left(t - \frac{T}{2}\right)\right] \sin\left[\omega\left(t - \frac{T}{2}\right)\right], \quad (5)$$

where ω is the average frequency, $\mathbf{E}_0$ is the maximum amplitude of the electric field, and T is the pulse duration. It is worth noting that in this paper we pay attention to the specially designed single-cycle laser pulses, whose center frequency and pulse duration are in a one-to-one correspondence by $\omega = \frac{12\hbar}{T}$, which allows us to concentrate the energy into a very short time interval, reducing the risk of detrimental scattering processes. Moreover, a single-cycle attosecond pulse, which minimizes its dephasing with the generated electron current density over an extended propagation, provides new opportunities for controlling electron motion in solids with unprecedented speed and accuracy. To characterize the ultrashort single-cycle pulse, we analyze the quantity $|E(\omega)|^2$ from the Fourier transformation of the electric field $E(t)$, i.e., $|E(\omega)|^2 = |\int dt E(t) e^{i\omega t}|^2$, which is proportional to the photon number density $N_{photon}(\omega) = \frac{c}{4\pi}|E(\omega)|^2/\hbar\omega$, as shown in Fig. 2 for three attosecond cases with duration $T_{as} = 0.1$ fs, $T_{as} = 0.3$ fs, and $T_{as} = 0.5$ fs, respectively, and two femtosecond cases $T_{fs} = 7$ fs and $T_{fs} = 9$ fs. Note that the shorter the pulse duration, the smaller the photon number density, the wider the photon spectral band. The broadening of the photon spectral band promises a much higher degree of attainable quantum interference because more pathways involving different frequency photons become accessible simultaneously, which is the foundation of lightwave electronics [57] based on attosecond pulses.
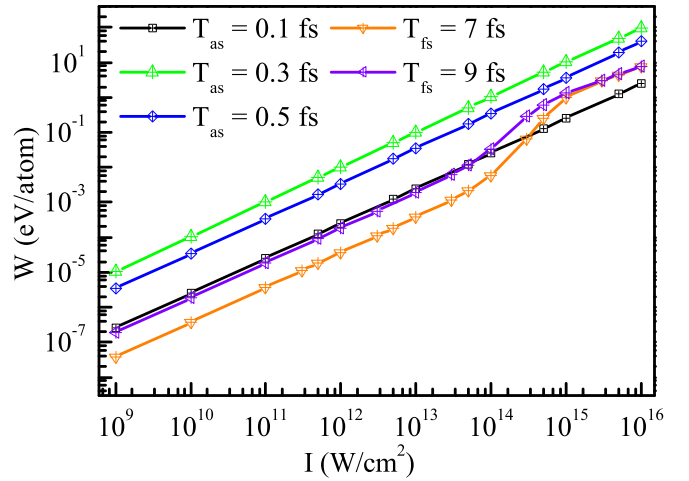

FIG. 3. After the end of the pulse, the energy transfer of each atom from single-cycle pulse to the diamond crystal represented by Eq. (6), under different pulse durations and peak intensities.

Figure 3 shows a series of energy transfer graphs from a single-cycle pulse to diamond crystal after the end of the pulse. The transferred energy $W(t)$ in the unit cell with volume of Ω can be expressed by the work done by the applied external field $E(t)$ as follows:

$$W(t) = \Omega \int_{-\infty}^{t} dt' \mathbf{E}(t') \cdot \mathbf{J}(t'). \quad (6)$$

The transferred energy of each atom is expressed as $W(\text{eV/atom}) = \lim_{t\to\infty} W(t)/N_{atom}$, where N_{atom} is the total number of atoms in the unit cell. For the femtosecond pulses, while single photon absorption process dominates at low intensity, multiphoton absorption process appears in the intensity region $10^{13} \leqslant I_{fs} \leqslant 3 \times 10^{15}$ W/cm^2. As the intensity increases further, the single photon absorption process is retained, which may be due to the saturation effect of the occupation. For shorter attosecond pulses, the absorption is always linearly dependent on the field intensity, and its slope is parallel to the femtosecond absorption curve at low intensity, which is a "one-photon" absorption process. Since the attosecond pulse consists of a wide energy range and low-density photons, the absorbed energy is the average of the one-photon absorption processes for different energies. These results indicate that the excitation mechanism in the attosecond timescale is different from that in the femtosecond timescale. In addition, since that the photon number density and the imaginary part of the dielectric function of diamond are both single-peak structures, from the linear response point of view, the closer their peaks are, the more overlapped the parts will be, leading to more energy transfer. However, it is interesting to see that the energy transfer is the maximum for $T_{as} = 0.3$ fs among all cases, rather than $T_{as} = 0.5$ fs, implying the appearance of the new effect in the interaction between attosecond light and matter, which is different from the traditional linear response mechanism.

Figure 4 further displays energy transfer and energy transfer rate with pulse duration, corresponding to a red line and a blue line, respectively. The upper axis is the average frequency
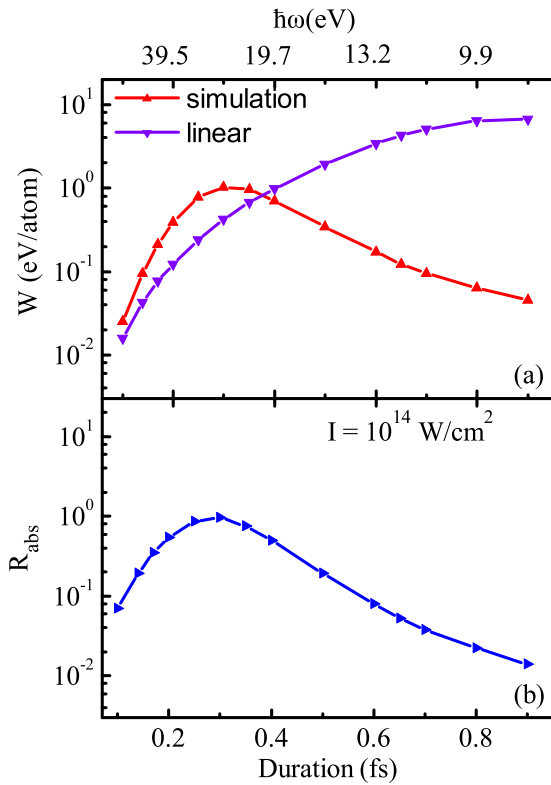
FIG. 4. After the end of the pulse, (a) the energy transfer of each atom from single-cycle pulse to the diamond crystal under different pulse durations. The red line represents the result of our simulation calculation. The violet line is the result of linear absorption calculated by Eq. (7). (b) The energy transfer rate of each atom in diamond crystal with various pulse durations. The upper axis is the average frequency ω corresponding to each pulse duration.

ω corresponding to each pulse duration. The energy transfer rate R_{abs} can be given by $W(eV/atom)/\Sigma$, where Σ is the total energy of the laser pulse, estimated by $\Sigma \propto \int \frac{c}{8\pi}E^2(t)dt$. No matter energy transfer or energy transfer rate, there is a maximum energy absorption value at $T_{as} = 0.3$ fs, which is consistent with Fig. 3. Besides, from a linear response point of view, the energy transfer can be defined as

$$W_{LR} \propto \int |E(\omega)|^2 \omega \, \text{Im} \, \varepsilon(\omega)d\omega, \qquad (7)$$

where $\text{Im} \, \varepsilon(\omega)$ is the imaginary part of the dielectric function. For comparison, we show the linear response results in Fig. 4 as violet lines. There is a deviation between our calculation simulation and linear absorption in energy transfer, which indicates that there is indeed a new effect between attosecond light and matter, compared to the traditional linear response absorption behavior.

In order to understand the difference in energy absorption observed in Fig. 3, we study absorbed energy $W(t)$ and current density $J(t)$ of diamond crystal at different times of a single-cycle light pulse duration with the laser intensity $I_{as} = 10^{14}$ W/cm^2 and $I_{as} = 10^{15}$ W/cm^2. As shown in Figs. 5(a$_1$)–5(a$_5$), it can be seen that as the attosecond pulse $E_{as}(t)$ evolves, the transferred energy $W(t)$ increases gradually, the maximum energy transfer occurs at $T_{as}(t) = 0.3$ fs after the pulse

ends. For the femtosecond pulse $E_{fs}(t)$, the transferred energy follows closely the oscillation of its corresponding pulse. In Figs. 5(a$_1$) and 5(a$_3$), periodic excitation and deexcitation are mainly influenced by the interaction of virtual excitation [58] and Rabi flopping [59], through Stark effect or multiphoton interference under resonant and nonresonant conditions. Virtual excitation largely means the distortion of the initial electronic state, while the Rabbi jump represents the oscillation of the number distribution between the valence band and the conduction band during the laser pulse irradiation. At the same time, as shown in Fig. 5(a$_1$) and Figs. 5(a$_3$)–5(a$_5$), there is an obvious reverse energy flow at the trailing edge of the laser pulse, which means part of the energy is transferred back to the radiation field.

When $T_{as} = 0.3$ fs, the electric current density $J(t)$ is in phase with the laser field $E(t)$ corresponding to the maximum energy transfer in Fig. 3 through Eq. (6), which is interpreted as the resonance energy transfer from an attosecond laser pulse to the material electronic system. When $T_{as} = 0.1$ fs, the phase of $J(t)$ lags behind $E(t)$, while the phase of $J(t)$ precedes $E(t)$ when $T_{as} = 0.5$ fs, so the phase shift results in less energy transfer according to Eq. (6), which is consistent with the phenomenon in Fig. 3. These differences may be caused by the fact that one and the same electron state in matter encounters all photons contained in an attosecond light pulse at the same time, enabling therefore interferences between pathways involving different intermediate states that are sensitive to the phase between these photons. However, for femtosecond pulses, as shown in Figs. 5(b$_4$) and 5(b$_5$), the phase of $J(t)$ is always obviously ahead of $E(t)$, and its phase difference is close to $\pi/2$, resulting in the smallest energy transferred from laser pulses to electrons.

According to Eq. (6) and the analysis of $J(t)$ and $W(t)$ in Fig. 5, it is clear that the attosecond laser pulse can make the current density resonate with the laser pulse by adjusting its duration, thereby maximizing the transfer energy. For convenience in the following discussion, the resonance situation of $T_{as} = 0.3$ fs is referred to as WZ type response, the pulse is referred to as T_{WZ}. The case where the current phase leads the pulse phase is called negative detuning (W type response), with the corresponding duration T_W, while the case where the current phase lags the pulse phase is called positive detuning (Z type response), and the corresponding duration is T_Z [60,61]. For femtosecond pulses at high intensity $I_{as} = 10^{15}$ W/cm^2, Fig. 5 clearly shows a low amplitude coherent oscillation of $J(t)$ at the trailing edge of the field due to the partial coherence left by the laser field between the involved nonstationary states, which is reminiscent of the plasma oscillation in metals [62] and consistent with the traditional nonlinear characteristics. For the attosecond pulse, with the increase of laser intensity, the current increases by corresponding multiples, exhibiting a linear response that dominates the response behavior, which is in accordance with the characteristics of the attosecond pulse with small photon number density.

Moreover, the above response can be vividly reflected in real-space presentation of the electron density difference in Figs. 6(b)–6(f). The ground state electron density is shown in Fig. 6(g). The red area indicates increasing of electron density, while blue indicates decreasing. There is a spatial
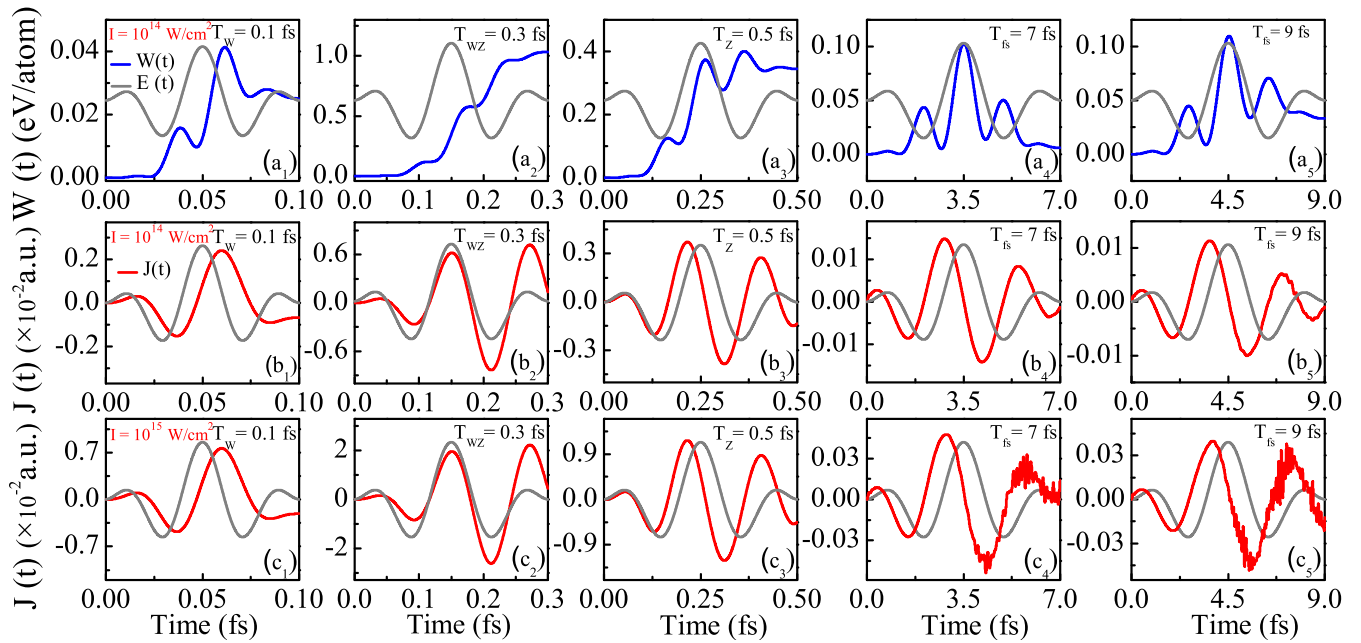
FIG. 5. The upper panels corresponds to the time-dependent energy transfer $W(t)$ induced by the single-cycle intense light pulses $E(t)$ in diamond crystal with intensity of $I_{as} = 10^{14}$ W/cm^2 and durations of $T(t) = 0.1$–9 fs, respectively. The gray solid lines show the scaled pulse $E(t)$. The middle and lower panels show the time-dependent electric current density $J(t)$ pumped by $E_{as-fs}(t)$ with intensity of $I_{as} = 10^{14}$ W/cm^2 and $I_{as} = 10^{15}$ W/cm^2, respectively.

region where the electron density difference changes the most compared to the ground state, which is the excitation out of the bonding orbitals, causing a decrease of the electron density around the bonds [63]. The picture for $T_{WZ} = 0.3$ fs shows the largest contrast with remarkable collective movement of electrons, while the $T_{fs} = 7$ fs is the smallest, which is consistent with the energy transfer in Fig. 3.

In order to understand the microscopic origin of these features, the change of occupation number is further analyzed with different laser intensity and pulse duration. Figure 7 shows the electronic density of state (DOS), occupied number

(OCC) in the ground state, and the difference of occupied number (DOO) between ground state and excited state in a unit cell of diamond crystal after the laser pulse. Figures 7(c)–7(e) show the results for attosecond pulses. The curves for intensities 10^{12} and 10^{14} W/cm^2 are multiplied by 10^3 and 10, respectively. Here we define that each DOO curve represents a transition mode. Surprisingly, both rescaled curves with weak light pulses of 10^{12} and 10^{14} W/cm^2 almost overlap with the DOO for 10^{15} W/cm^2. That means the transition mode is sensitive to the duration of the attosecond pulse, but insensitive to the intensity up to a scaling factor. However, in the case
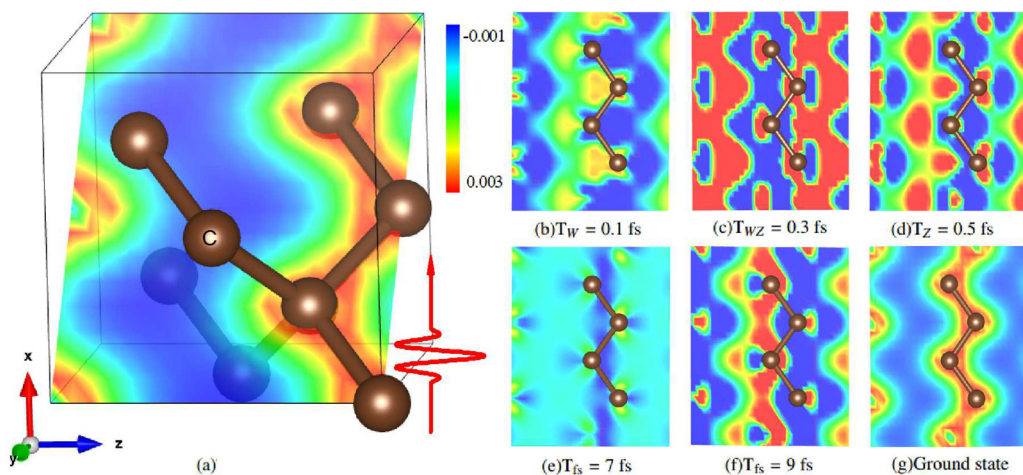

FIG. 6. (a) The schematic diagram of the calculated diamond crystal structure. The colored surface is the section [1, −1, 0] selected later. (b)–(f) The electron density difference distribution in diamond crystal pumped by the single-cycle intense light pulses with $I_{as} = 10^{15}$ W/cm^2 and $T = 0.1$–9 fs, respectively. (g) The ground state electron density. Red area indicates increasing of electron density, while blue indicates decreasing.
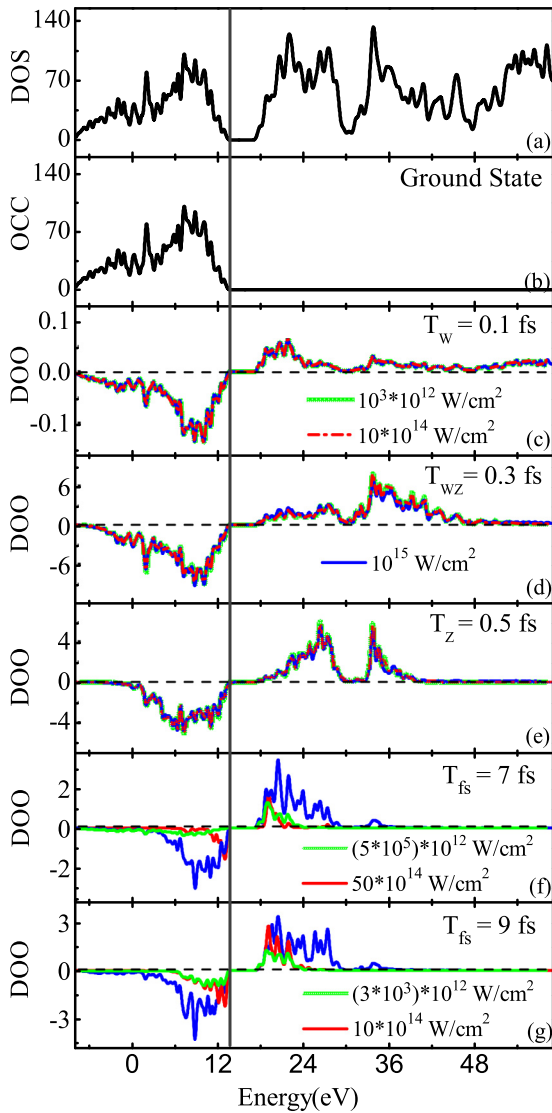
FIG. 7. The electronic density of states (DOS), occupation number (OCC) in an unit cell of diamond crystal at ground state, and after the laser pulse ends, the difference of occupation number (DOO) between ground state and excited state under varying pulse duration and peak intensity. The vertical solid line in the panel indicates the Fermi level E_F and the gray dashed line represents the zero line. The DOOs under lower intensity pulse are rescaled.

of femtosecond pulses, the rescaled curves do not overlap with each other due to typical nonlinear effect, as shown in Figs. 7(f) and 7(g), which is consistent with the intensity-related energy transfer curve in Fig. 3. The maximum DOO of $T_{WZ} = 0.3$ fs corresponds to the maximum excitation, as observed in Fig. 3 for the maximum energy transfer. Comparing the curves for the attosecond cases, the DOO spectrum of $T_W = 0.1$ fs extends to higher excitations in the conduction band, as seen from Fig. 7(c). That is because the photon number density distribution for $T_W = 0.1$ fs is the widest as shown in Fig. 2, and higher electronic states in matter become accessible. In general, on the one hand, because the photon number density of each frequency contained in the attosecond pulse is very small, the interaction between attosecond pulse

light and matter shows the single-photon linear response behavior with the pulse intensity below 10^{16} W/cm^2. On the other hand, because the attosecond light pulse has a wide spectral band of photons, different combinations of a quantum pathway can have dynamical interferences [64,65]. The final occupation number of electron states is determined by the dynamic interference of the different quantum pathways. The dynamic interference can be constructive or destructive. By introducing dynamical interferences, it is possible to alter the classical linear response behavior, for example, the dark light pulse which have the same spectral content as a conventional pulse but are not absorbed by conventional absorbing media as an extreme case. More importantly, because these quantum transition paths, generated by an attosecond light pulse, are completely coherent, the interference structure in DOO records the phase information of the quantum transition path. Hence, we refer to this new effect in the interaction between attosecond light and matter as the linear dynamic interference response mechanism, in order to be different from the traditional linear response mechanism.

B. Light propagation through a diamond thin film

Then, in this section, we investigate the behavior of spatial propagation of the single-cycle light pulses passing a free-standing diamond thin film in the second level of the model. For the incident pulse, it propagates along the x axis, and its polarization direction is along the z axis. The wave form is as follows:

$$\mathbf{A}_X(t) = -\frac{\mathbf{E}_0}{\omega} \cos^2\left(\frac{\pi(X - ct)}{cT}\right) \sin\left(\frac{\omega(X - ct)}{c}\right). \quad (8)$$

Various snapshots of simulated attosecond laser pulses incident on the diamond thin films are shown in Figs. 8 and 9. The pulse intensity is $I_{as} = 10^{15}$ W/cm^2 (maximum amplitude is 0.169 a.u.). The thickness of diamond film is set to $d = 29.988$ nm. Since the lattice constant of diamond is about 0.357 nm the thickness is the size of 84 lattices. Figure 8(a$_1$) shows the distribution of the incident pulse in the film. Figures 8(a$_2$)–8(a$_4$) correspond to the snapshots for attosecond pulses with durations of $T_W = 0.1$ fs, $T_{WZ} = 0.3$ fs, and $T_Z = 0.5$ fs, respectively. The femtosecond cases are shown in Figs. 8(a$_5$) and 8(a$_6$). The distribution of absorption energy (W_{abs}) of 0.1–9 fs in the diamond film is shown in Fig. 9. The gray area ($0 < X < 29.988$ nm) represents the diamond thin film, and the area where $X < 0$ and $X > 29.988$ nm represents the vacuum. When the attosecond pulse evolves at $t = 6$ T, the incident laser pulse has been completely separated into the reflection component (vacuum region on the left side of the diamond film) and the transmission component (vacuum region on the right side of the diamond film), while for the femtosecond pulse it is $t = 2$ T. The reflection occurs on the front and back surfaces of the film, mainly the front surface, because many conduction band (CB) electrons exist there. On the whole, the results show that the diamond films have obvious different shaping effects on the above three attosecond pulses, which is clearly different from the femtosecond pulse, and the energy deposited in the diamond film increases greatly with the increase of pulse duration.
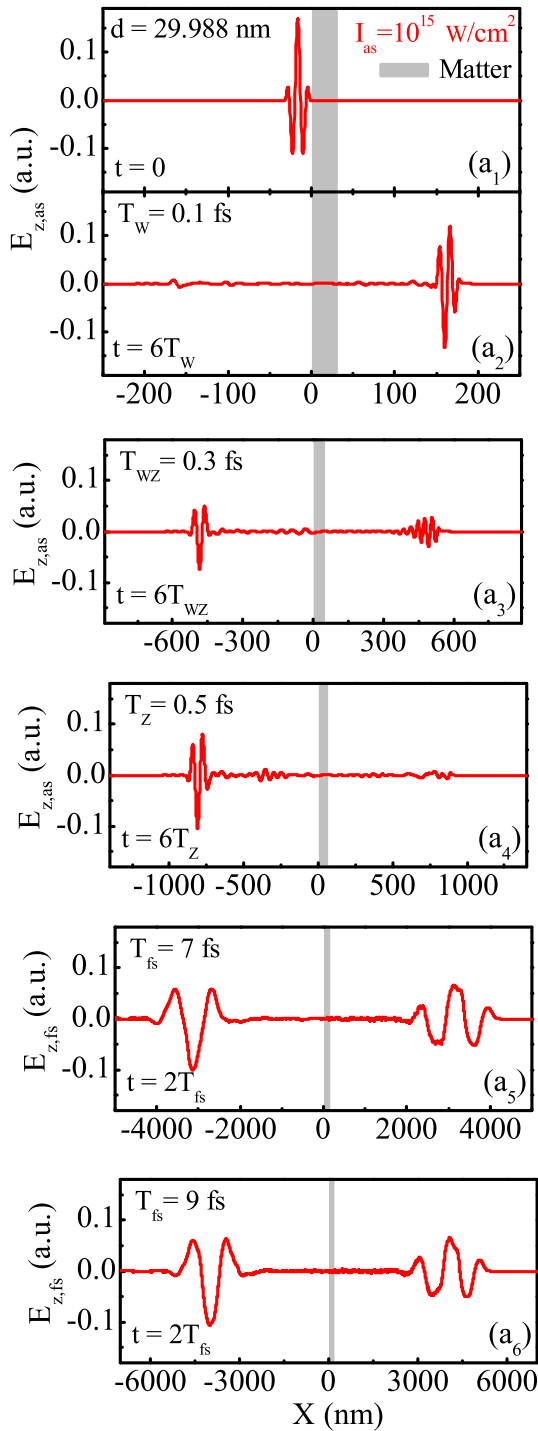
FIG. 8. (a$_1$) At the initial moment ($t = 0$), the distribution of electric field ($E_{Z,as}$) in space. (a$_2$)–(a$_4$) At $t = 6$ T, the distribution of electric field ($E_{Z,as}$) in space with three different types of attosecond single-cycle laser pulses ($T_W = 0.1$ fs, $T_{WZ} = 0.3$ fs, and $T_Z = 0.5$ fs, respectively). (a$_5$) and (a$_6$) The distribution of electric field ($E_{Z,fs}$) at $t = 2$ T in space with femtosecond pulse of $T_{fs} = 7$ fs and $T_{fs} = 9$ fs, respectively. The laser pulse with a peak intensity of $I_{as} = 10^{15}$ W/cm^2 transmits perpendicular to the diamond film with thickness of $d = 29.988$ nm. The gray area ($0 < X < 29.988$ nm) represents the diamond film, and the area where $X < 0$ and $X >$ 29.988 nm represents the vacuum.
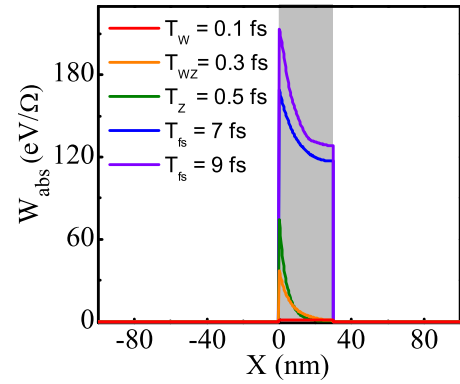

FIG. 9. Corresponding to the laser parameters in Fig. 8, the distribution of absorption energy (W_{abs}) in the diamond film.

As shown in Fig. 8(a$_2$), when $T_W = 0.1$ fs, the incident laser pulse at $t = 0$ starts to propagate at $X = -32$ nm relative to the diamond film surface at $X = 0$. In addition, because of the $T_W = 0.1$ fs wide frequency spectrum, it can tunnel through the thin plasma and radiate into vacuum, so it is obvious that there is a strong transmission pulse field in the region of $145 < X < 185$ nm at $t = 6T_W$, and the reflected field is almost zero. The maximum amplitude of the transmitted field is close to the amplitude of the incident field, and the shape of the transmitted field has changed compared to the wave form of the incident field, showing a distinct shaping effect. Due to the short duration of the W-shaped pulse, its interaction time with the material is short, and the energy deposited in the film is small, as shown in Fig. 9. After the laser pulse ends, the electronic state of the system returns to the ground state, which provides the idea of nondestructive irradiation of the laser.
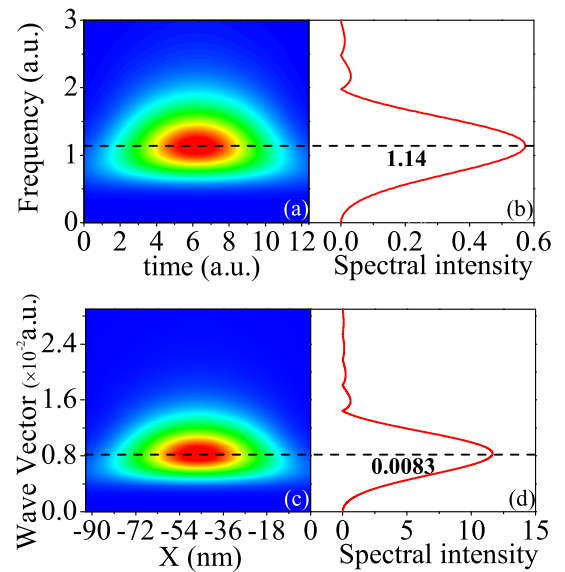

FIG. 10. (a) Time-frequency representation obtained by using a Morlet transform, (b) frequency distribution spectrum, (c) space-wave-vector representation obtained by using a Morlet transform, and (d) wave-vector distribution spectrum, of the incident electric field with the peak intensity of 10^{15} W/cm^2 and $T_{WZ} = 0.3$ fs.
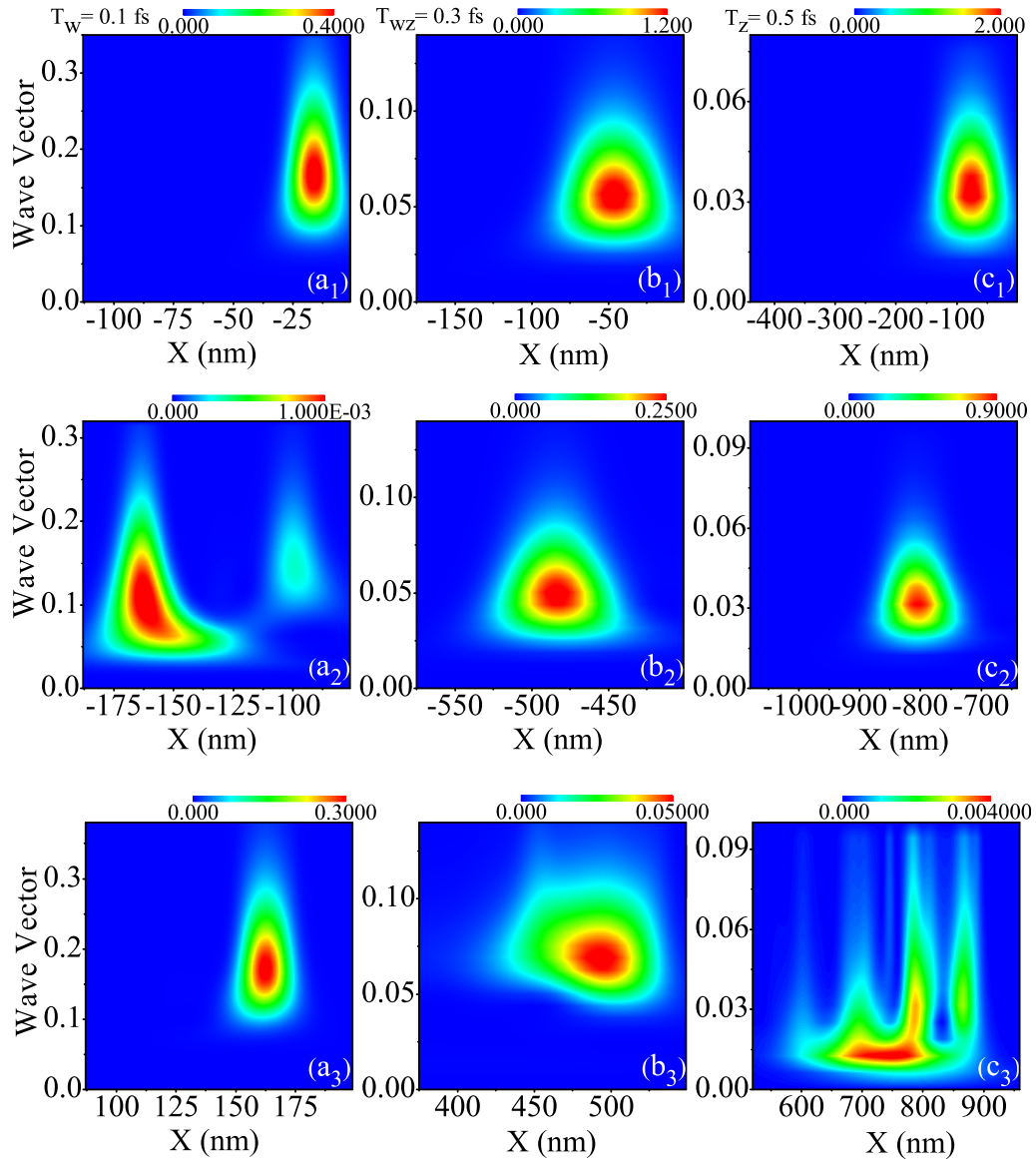
FIG. 11. Morlet transformations of the spatial distribution of the incident fields with the peak intensity of 10^{15} W/cm^2 and three different types of attosecond laser pulses ($T_W = 0.1$ fs, $T_{WZ} = 0.3$ fs, and $T_Z = 0.5$ fs) correspond to the upper panels (a$_1$)–(c$_1$), respectively. Morlet transformations of the reflected fields and the transmitted fields correspond to the middle panels (a$_2$)–(c$_2$) and the lower panels (a$_3$)–(c$_3$), respectively.

For $T_{WZ} = 0.3$ fs, it can be seen from Fig. 8(a$_3$), when $t = 6T_{WZ}$, both reflection field and transmission field can be observed, the reflection wave has a π phase difference relative to the incident wave, and the wave form of the transmitted wave is modulated and its wavelength is about 220 nm. Moreover, the transmitted wave has a relatively flat electric field envelope, showing chirp effect: stretching at its front and converging at its end. The energy absorbed by the diamond film increases, which is more than 8 times the absorbed energy of $T_W = 0.1$ fs, and the reflected and transmitted electromagnetic field energy W_{emf} decreases relative to the incident field. It can also be noted that most of the energy is deposited in the diamond film, and the deposition rate decreases with the increase of the film depth from Fig. 9. The remaining small part of the energy is mainly left in the reflected field.

When the Z-type laser pulse ($T_Z = 0.5$ fs) is vertically incident on the diamond film, as shown in Fig. 8(a$_4$), the absorbed energy near the diamond film surface is about 11 times as much as that of $T_W = 0.1$ fs, the wave form of the transmission field almost disappears and the energy W_{emf} of the transmission field tends to zero. However, it has the characteristics of strong reflection (maximum amplitude is 0.105 a.u.) and absorption. It can be seen from Fig. 9 that a large amount of energy is deposited inside the diamond film, which may cause material damage. Besides, the energy is mainly deposited near the surface (olive solid line) and the transferred energy density rapidly decays inside the film. This transfer of energy drives the subsequent atomic motion and further induces laser induced damage, such as melting and laser ablation.

Figures 8(a_5)–8(a_6) are the snapshots of the femtosecond pulses with pulse durations of 7 and 9 fs, respectively. The two figures are very similar, both have a reflected field and a transmitted field, the transmitted wave form is similar to that of the incident field, and the reflected field exhibits a phase shift of π. Obviously the thin film cannot achieve shaping effect with the femtosecond laser pulse wave form. From Fig. 9, for femtosecond pulses, as the duration increases, the nonlinear electronic dynamics effect is more obvious due to the increase in the interaction time between the material and the intense laser, resulting in a large amount of energy being deposited inside the diamond film, which may cause damage to the material.

In order to understand the spatial distribution of the reflected and transmitted electric field, wavelet transform is applied to the signal. Wavelet analysis is a powerful tool for signal processing, in which the mother wavelet is defined as

$$m(x) = e^{i \cdot x} e^{-x^2/2\sigma^2}, \tag{9}$$

and a child wavelet is defined by expanding and transforming with k and x_1, respectively as follows:

$$W_{k,x_1}(x) = e^{ik(x-x_1)} e^{-k^2(x-x_1)^2/2\sigma^2}. \tag{10}$$

The Morlet transform of signal $E(x)$ is expressed by

$$M_{k,x_1} = \left| \int \frac{1}{\sqrt{\sigma}} E(x) W_{k,x_1}(x) dx \right|^2. \tag{11}$$

Parameter σ determines the size of the temporal window. The space and wave vector resolution can be balanced by adjusting the value of σ of the Morlet wavelet. Decreasing σ will decrease the wave vector resolution but it will increase the space resolution. When σ approaches 0, the Morlet wavelet becomes a Dirac function with optimal space resolution, while when σ tends to infinity, the Morlet wavelet becomes a plane wave function with optimal wave vector resolution. Therefore, for a certain signal, there is always an optimal σ with the finest resolution for both space and wave vector.

In Fig. 10, for the pulse electric field with the peak intensity of 10^{15} W/cm^2 and pulse duration of $T_{WZ} = 0.3$ fs used in this paper, by comparing the Morlet transform in the time-frequency plane and the space-wave vector plane, the value of σ is selected as 0.5 for a suitable value to balance the time (space) and frequency (wave vector) resolution. Therefore, $\sigma = 0.5$ is chosen for the subsequent study. In addition, it can also be obtained that the center frequency of the pulse electric field is 1.14, and the center wave vector is 0.0083 through the formula transformation $k = \omega/c$, where c is 137. The values 1.14 and 0.0083 are shown in Figs. 10(b) and 10(d).

As shown in Fig. 11, when the reflected field $\mathbf{E}_R$ and the transmitted field $\mathbf{E}_T$ are completely separated, Morlet transformation of the spatial distribution of the incident fields with the peak intensity of 10^{15} W/cm^2 and three different types of attosecond laser pulses ($T_W = 0.1$ fs, $T_{WZ} = 0.3$ fs, and $T_Z = 0.5$ fs) corresponds to the upper panels of Figs. 11(a_1)–11(c_1), respectively. Morlet transformation of the corresponding reflected field and the transmitted field corresponds to the middle panels of Figs. 11(a_2)–11(c_2) and the lower panels of Figs. 11(a_3)–11(c_3), respectively.
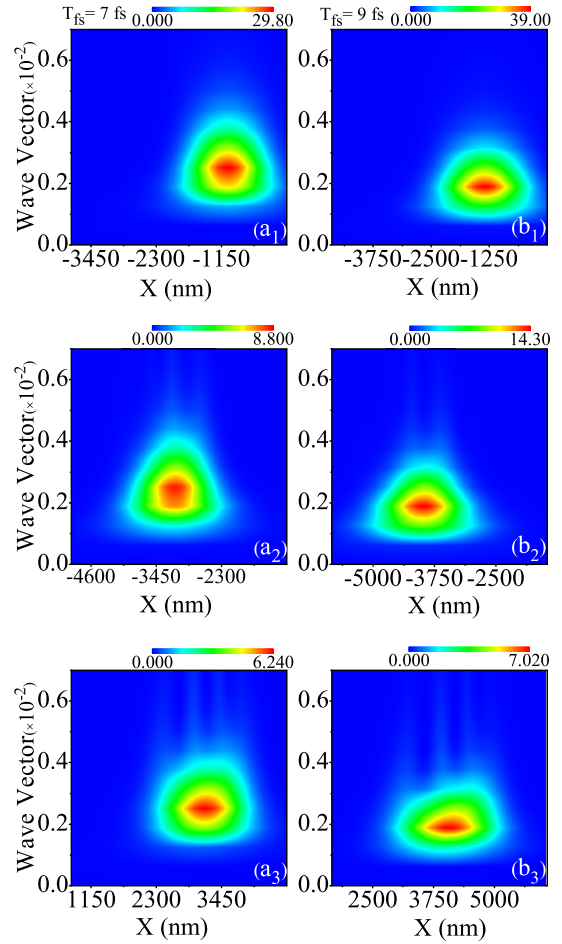

FIG. 12. Similar to Fig. 14, Morlet transformations of the spatial distribution of the incident fields, the reflected fields, and the transmitted fields with femtosecond pulse of $T_{fs} = 7$ fs and $T_{fs} = 9$ fs and the peak intensity of 10^{15} W/cm^2.

From the results of Fig. 11, we can intuitively find that there is a strong transmission and weak reflection in the case of $T_W = 0.1$ fs, strong transmission and strong reflection for $T_{WZ} = 0.3$ fs, and strong reflection and weak transmission for $T_Z = 0.5$ fs. Besides, the possible chirps of transmission and reflection pulses are shown in Figs. 11(a_2) and 11(b_3), respectively, and the broadband XUV light has been built up during the propagation of the driving attosecond pulse through the diamond film as seen in Fig. 11(c_3). Hence, the diamond film has shaping effects on attosecond pulses. For comparison, Morlet transformations of the spatial distribution of the incident fields, the reflected fields, and the transmitted fields with femtosecond pulse of $T_{fs} = 7$ fs and $T_{fs} = 9$ fs are shown in Fig. 12. It can be seen that the Morlet transformations of the incident fields, the reflected fields, and the transmitted fields for femtosecond pulse are relatively stable in shape.

Another interesting phenomenon is shown in Fig. 13. For attosecond pulses, the line shape of the electric field seems insensitive to the pulse intensity. Taking the pulse duration of $T_{WZ} = 0.3$ fs for example, the line shapes of the electric field in diamond film with thickness of $d = 29.988$ nm under different laser intensities of 10^{15}, 10^{14}, and 10^9 W/cm^2, over-
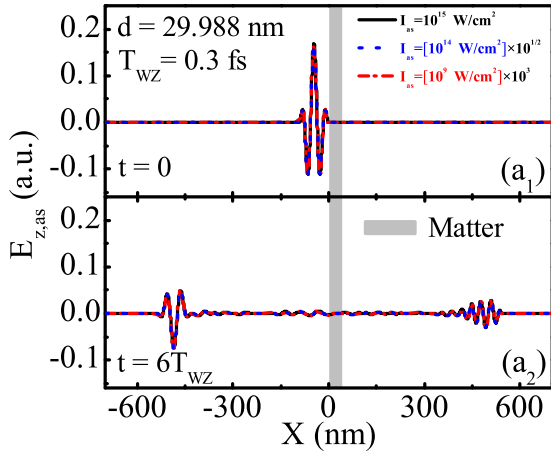
FIG. 13. The spatial distribution of electric field ($E_{Z,as}$) of diamond film with $d = 29.988$ nm under the attosecond light pulse of $T_{WZ} = 0.3$ fs and different laser intensity. The electric fields of lower intensities are rescaled.

lap with each other after being multiplied by proper scaling factors. For femtosecond pulses, as shown in Fig. 14, when the laser intensity is weak, the lines for the laser intensities of 10^9 and 10^{10} W/cm^2 overlap each other after multiplying 10^3 and $10^{5/2}$, respectively. But when the intensities increase to 10^{14} and 10^{15} W/cm^2, the lines cannot bring to each other by simple scaling, which indicates the emergence of nonlinear effect. Therefore, consistent with the discussion in Sec. III A, the propagation behavior of an attosecond pulse in the thin film is independent of laser intensity, which is a characteristic different from a femtosecond pulse.

Finally, we show reflection, transmission, and absorption rates as a function of diamond film thickness with three different types of attosecond laser pulses ($T_W = 0.1$ fs, $T_{WZ} = 0.3$ fs, and $T_Z = 0.5$ fs in Fig. 15 when the reflected and the transmitted pulses are well separated. The peak intensity is 10^{15} W/cm^2. The reflection rate $\mathfrak{R}$ and transmission rate $\mathcal{T}$ of the material is defined by the ratio of the total electro-
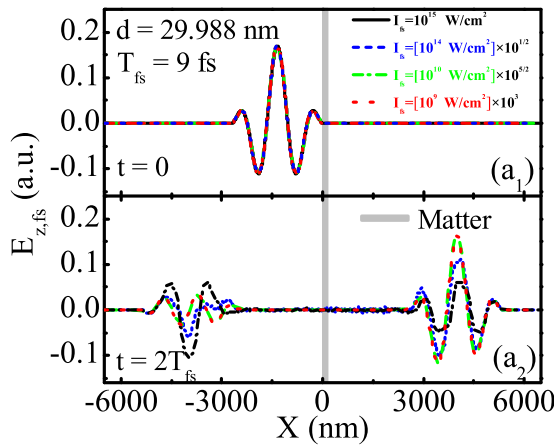

FIG. 14. The spatial distribution of electric field ($E_{Z,fs}$) of diamond film with $d = 29.988$ nm under the femtosecond light pulse of $T_{fs} = 9$ fs and different laser intensity. The electric fields of lower intensities are rescaled.
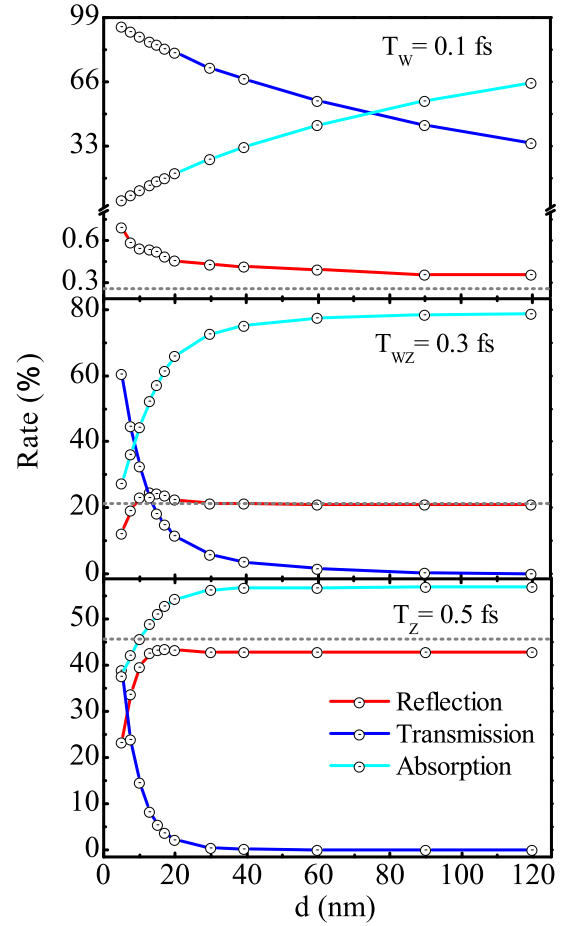

FIG. 15. Reflection, transmission, and absorption rates as a function of diamond film thickness with the peak intensity of 10^{15} W/cm^2 and three different types of laser pulses ($T_W = 0.1$ fs, $T_{WZ} = 0.3$ fs, and $T_Z = 0.5$ fs). The gray dotted line represents the total reflectivity of the linear response.

magnetic energy of reflected and transmitted waves to the electromagnetic energy of incident waves, respectively, and the absorption rate $\mathcal{A}$ is given by $\mathcal{A} = 1 - \mathfrak{R} - \mathcal{T}$. From Fig. 15, as the thin film thickness increases, more and more energy is deposited in the thin film. At the beginning, the absorption rate $\mathcal{A}$ increases and the corresponding transmittance $\mathcal{T}$ decreases, but when it reaches a critical thickness, they start to saturate. For the pulse durations of $T_{WZ} = 0.3$ fs and $T_Z = 0.5$ fs, the reflection rate $\mathfrak{R}$ first rapidly increases and then decreases and saturates. For $T_W = 0.1$ fs, the reflectivity is relatively small. Taken together, as the pulse duration increases, absorption increases and transmission decreases. It should also be pointed out here that the conduction band (CB) electrons generated in the thin film absorb and reflect laser pulses, which leads to the change of interference conditions and plays a leading role in determining the reflectivity of the thin film. As the thickness of the thin film increases, the CB electrons generated around the front and back surfaces change the interference condition in a way that adversely affects reflectivity. In addition, because of finite pulse duration, the broad spectrum of laser pulse will affect the interference conditions, thus affecting the reflection coefficient and reduc-

ing the reflectivity [66]. The final convergence of reflectivity implies that the CB electrons, mainly generated at the front surface, play a dominant role in the bringing about changes of reflectivity.

With the increase of film thickness, it approaches the traditional classical model of linear response. For comparison, the total reflectivity $\mathfrak{R}_{\text{LR}}$ of linear response is given in each panel by gray dotted lines, which is defined as

$$\mathfrak{R}_{\text{LR}} = \frac{\int R(\omega)|E(\omega)|^2 d\omega}{\int |E(\omega)|^2 d\omega}, \tag{12}$$

where $R(\omega)$ is the reflectivity, evaluated by the following equation using dielectric function $\varepsilon(\omega)$:

$$R(\omega) = \left| \frac{\sqrt{\varepsilon(\omega)} - 1}{\sqrt{\varepsilon(\omega)} + 1} \right|^2. \tag{13}$$

Interestingly, for $T_{\text{WZ}} = 0.3$ fs, with the increase of film thickness, the reflectance saturation value approaches the total reflectance value $\mathfrak{R}_{\text{LR}}^{0.3\,\text{fs}}$ of linear response, and the reflectance saturation value of $T_{\text{W}} = 0.1$ fs is above $\mathfrak{R}_{\text{LR}}^{0.1\,\text{fs}}$, while that of $T_{\text{Z}} = 0.5$ fs is below $\mathfrak{R}_{\text{LR}}^{0.5\,\text{fs}}$, indicating the linear dynamic interference response mechanism.

IV. CONCLUSIONS

In conclusion, interestingly enough, on account of the ultrashort duration of attosecond light pulses, its interaction with matter is distinguished from conventional long light pulses. We propose and demonstrate a mechanism and phenomenon of linear dynamic interference response between attosecond light pulse and matter. Our simulations show that the interaction of single-cycle light pulses of duration 0.1 to 0.5 fs (or 100–500 as) with diamond crystal and thin film has distinct features, which indicates a linear scaling behavior with the pulse intensity below 10^{16} W/cm^2 on the one hand and an unusual linear dynamic interference response behavior with the pulse width, determined by the interference of the different quantum pathways on the other hand.

As a final note, while on the one hand this type of research is important from a fundamental point of view as it can provide important insights into the complex interaction between attosecond light pulse and matter in previously unexplored regimes of parameters where electron correlation, collective effects, matter characteristics, phase between photons contained in an attosecond light pulse, and film geometries becomes increasingly important, on the other hand, this research also comprises considerable potential for applications in designing devices of shaping attosecond light pulses, which deserves to be investigated in future research both theoretically and experimentally.

[1] M. Hentschel, R. Kienberger, C. Spielmann, G. A. Reider, N. Milosevic, T. Brabec, P. Corkum, U. Heinzmann, M. Drescher, and F. Krausz, Attosecond metrology, Nature (London) **414**, 509 (2001).

[2] G. Sansone, E. Benedetti, F. Calegari, C. Vozzi, L. Avaldi, R. Flammini, L. Poletto, P. Villoresi, C. Altucci, R. Velotta *et al.*, Isolated single-cycle attosecond pulses, Science **314**, 443 (2006).

[3] E. Goulielmakis, M. Schultze, M. Hofstetter, V. S. Yakovlev, J. Gagnon, M. Uiberacker, A. L. Aquita, E. M. Gullikson, D. T. Attwood, and R. Kienberger, Single-cycle nonlinear optics, Science **320**, 1614 (2008).

[4] M. J. Abel, T. Pfeifer, P. M. Nagel, W. Boutu, M. J. Bell, C. P. Steiner, D. M. Neumark, and S. R. Leone, Isolated attosecond pulses from ionization gating of high-harmonic emission, Chem. Phys. **366**, 9 (2009).

[5] F. Ferrari, F. Calegari, M. Lucchini, C. Vozzi, S. Stagira, G. Sansone, and M. Nisoli, High-energy isolated attosecond pulses generated by above-saturation few-cycle fields, Nat. Photon. **4**, 875 (2010).

[6] K. Zhao, Q. Zhang, M. Chini, Y. Wu, X. Wang, and Z. Chang, Tailoring a 67 attosecond pulse through advantageous phase-mismatch, Opt. Lett. **37**, 3891 (2012).

[7] F. Frank, C. Arrell, T. Witting, W. Okell, J. McKenna, J. Robinson, C. Haworth, D. Austin, H. Teng, I. Walmsley *et al.*, Invited review article: Technology for attosecond science, Rev. Sci. Instrum. **83**, 52 (2012).

[8] E. J. Takahashi, P. Lan, O. D. Mücke, Y. Nabekawa, and K. Midorikawa, Attosecond nonlinear optics using gigawatt-scale isolated attosecond pulses, Nat. Commun. **4**, 2691 (2013).

[9] T. J. Hammond, G. G. Brown, K. T. Kim, D. M. Villeneuve, and P. B. Corkum, Attosecond pulses measured from the attosecond lighthouse, Nat. Photonics **10**, 171 (2016).

[10] J. Li, X. Ren, Y. Yin, K. Zhao, A. Chew, Y. Cheng, E. Cunningham, Y. Wang, S. Hu, Y. Wu *et al.*, 53-attosecond x-ray pulses reach the carbon K-edge, Nat. Commun. **8**, 186 (2017).

[11] T. Gaumnitz, A. Jain, Y. Pertot, M. Huppert, I. Jordan, F. Ardana-Lamas, and H. J. Wörner, Streaking of 43-attosecond soft-x-ray pulses generated by a passively CEP-stable mid-infrared driver, Opt. Express **25**, 27506 (2017).

[12] X. Ren, J. Li, Y. Yin, K. Zhao, A. Chew, Y. Wang, S. Hu, Y. Cheng, E. Cunningham, Y. Wu *et al.*, Attosecond light sources in the water window, J. Opt. **20**, 023001 (2018).

[13] Y. X. Zhang, S. Rykovanov, M. Shi, C. L. Zhong, X. T. He, B. Qiao, and M. Zepf, Giant Isolated Attosecond Pulses from Two-Color Laser-Plasma Interactions, Phys. Rev. Lett. **124**, 114802 (2020).

[14] J. W. Wang, M. Zepf, and S. G. Rykovanov, Intense attosecond pulses carrying orbital angular momentum using laser plasma interactions, Nat. Commun. **10**, 5554 (2019).

[15] A. Wirth, E. Goulielmakis, Z.-H. Loh, R. Santra, N. Rohringer, V. S. Yakovlev, S. Zherebtsov, T. Pfeifer, A. M. Azzeer, M. F. Kling, S. R. Leone, and F. Krausz, Attosecond transient absorption spectroscopy for real-time observation of valence electron

motion, in *International Conference on Ultrafast Phenomena* (Optical Society of America, Washington, DC, 2010), p. WE1.

[16] P. Johnsson, J. Mauritsson, T. Remetter, A. L'Huillier, and K. J. Schafer, Attosecond Control of Ionization by Wave-Packet Interference, Phys. Rev. Lett. **99**, 233001 (2007).

[17] H. Wang, M. Chini, S. Chen, C. H. Zhang, F. He, Y. Cheng, Y. Wu, U. Thumm, and Z. Chang, Attosecond Time-Resolved Autoionization of Argon, Phys. Rev. Lett. **105**, 143002 (2010).

[18] K. Klünder, J. M. Dahlström, M. Gisselbrecht, T. Fordell, M. Swoboda, D. Guénot, P. Johnsson, J. Caillat, J. Mauritsson, A. Maquet, R. Taïeb, and A. L'Huillier, Probing Single-Photon Ionization on the Attosecond Time Scale, Phys. Rev. Lett. **106**, 143002 (2011).

[19] P. Eckle, A. N. Pfeiffer, C. Cirelli, A. Staudte, R. Dörner, H. G. Muller, M. Büttiker, and U. Keller, Attosecond ionization and tunneling delay time measurements in helium, Science **322**, 1525 (2008).

[20] M. Drescher, M. Hentschel, R. Kienberger, M. Uiberacker, V. Yakovlev, A. Scrinzi, T. Westerwalbesloh, U. Kleineberg, U. Heinzmann, and F. Krausz, Time-resolved atomic inner-shell spectroscopy, Nature (London) **419**, 803 (2002).

[21] M. Ossiander, F. Siegrist, V. Shirvanyan, R. Pazourek, A. Sommer, T. Latka, A. Guggenmos, S. Nagele, J. Feist, J. Burgdörfer, R. Kienberger, and M. Schultze, Attosecond correlation dynamics, Nat. Phys. **13**, 280 (2017).

[22] M. Uiberacker, T. Uphues, M. Schultze, A. J. Verhoef, V. Yakovlev, M. F. Kling, J. Rauschenberger, N. M. Kabachnik, H. Schröder, M. Lezius *et al.*, Attosecond real-time observation of electron tunnelling in atoms, Nature (London) **446**, 627 (2007).

[23] Y. Cheng, M. Chini, X. Wang, A. Gonzalezcastrillo, A. Palacios, L. Argenti, F. Martin, and Z. Chang, Reconstruction of an excited-state molecular wave packet with attosecond transient absorption spectroscopy, Phys. Rev. A **94**, 023403 (2016).

[24] M. Reduzzi, W-C. Chu, C. Feng, A. Dubrouil, J. Hummert, F. Calegari, F. Frassetto, L. Poletto, O. Kornilov, M. Nisoli *et al.*, Observation of autoionization dynamics and sub-cycle quantum beating in electronic molecular wave packets, J. Phys. B: At. Mol. Opt. Phys. **49**, 065102 (2016).

[25] E. R. Warrick, W. Cao, D. M. Neumark, and S. R. Leone, Probing the dynamics of Rydberg and valence states of molecular nitrogen with attosecond transient absorption spectroscopy, J. Phys. Chem. A **120**, 3165 (2016).

[26] F. Calegari, D. Ayuso, A. Trabattoni, L. Belshaw, S. De Camillis, S. Anumula, F. Frassetto, L. Poletto, A. Palacios, P. Decleva, J. B. Greenwood, F. Martín, and M. Nisoli, Ultrafast electron dynamics in phenylalanine initiated by attosecond pulses, Science **346**, 336 (2014).

[27] Y. Nabekawa, Y. Furukawa, T. Okino, A. Amani Eilanlou, E. J. Takahashi, K. Yamanouchi, and K. Midorikawa, Sub-10-fs control of dissociation pathways in the hydrogen molecular ion with a few-pulse attosecond pulse train, Nat. Commun. **7**, 12835 (2016).

[28] G. Sansone, F. Kelkensberg, J. F. Pérez-Torres, F. Morales, M. F. Kling, W. Siu, O. Ghafur, P. Johnsson, M. Swoboda, E. Benedetti *et al.*, Electron localization following attosecond molecular photoionization, Nature (London) **465**, 763 (2010).

[29] S. Haessler, J. Caillat, W. Boutu, C. Giovanetti-Teixeira, T. Ruchon *et al.*, Attosecond imaging of molecular electronic wavepackets, Nat. Phys. **6**, 200 (2010).

[30] B. Förg, J. Schötz, F. Sümann, M. Küger, B. Ahn, W. A. Okell, K. Wintersperger, S. Zherebtsov, A. Guggenmos *et al.*, Attosecond nanoscale near-field sampling, Nat. Commun. **7**, 11717 (2016).

[31] M. Krüger, M. Schenk, and P. Hommelhoff, Attosecond control of electrons emitted from a nanoscale metal tip, Nature (London) **475**, 78 (2011).

[32] S. Neppl, R. Ernstorfer, A. L. Cavalieri, C. Lemell, G. Wachter *et al.*, Direct observation of electron propagation and dielectric screening on the atomic length scale, Nature (London) **517**, 342 (2015).

[33] A. Schiffrin, T. Paasch-Colberg, N. Karpowicz, V. Apalkov, D. Gerster, S. Mühlbrandt, M. Korbman, J. Reichert, M. Schultze, S. Holzner, J. V. Barth, R. Kienberger, R. Ernstorfer, V. S. Yakovlev, M. I. Stockman, and F. Krausz, Optical-field-induced current in dielectrics, Nature (London) **493**, 70 (2013).

[34] F. Schlaepfer, M. Lucchini, S. A. Sato, M. Volkov, L. Kasmi, N. Hartmann, A. Rubio, L. Gallmann, and U. Keller, Attosecond optical-field-enhanced carrier injection into the GaAs conduction band, Nat. Phys. **14**, 560 (2018).

[35] L. Jiang, A.-D. Wang, B. Li, T.-H. Cui, and Y.-F. Lu, Electrons dynamics control by shaping femtosecond laser pulses in micro/nanofabrication: modeling, method, measurement and application, Light Sci. Appl. **7**, 17134 (2018).

[36] R. Stoian, M. Wollenhaupt, T. Baumert, and I. V. Hertel, Temporal pulse tailoring in ultrafast laser manufacturing technologies, in *Laser Precision Microfabrication*, edited by K. Sugioka, M. Meunier, and A. Piqué (Springer, Berlin, 2010), pp. 121–144.

[37] R. López-Martens, K. Varjú, P. Johnsson, J. Mauritsson, Y. Mairesse, P. Salières, M. B. Gaarde, K. J. Schafer, A. Persson, S. Svanberg, C. G. Wahlström, and A. L'Huillier, Amplitude and Phase Control of Attosecond Light Pulses, Phys. Rev. Lett. **94**, 033001 (2005).

[38] E. Gustafsson, T. Ruchon, M. Swoboda, T. Remetter, E. Pourtal, R. López-Martens, P. Balcou, and A. L'Huillier, Broadband attosecond pulse shaping title, Opt. Lett. **32**, 1353 (2007).

[39] A. Guggenmos, M. Hofstetter, R. Rauhut, C. Späth, S. Hertrich, B. Nickel, S. Yang, E. M. Gullikson, J. Schmidt, and M. Seibald, Broadband multilayer mirror and diffractive optics for attosecond pulse shaping in the 280–500 eV photon energy range, EPJ Web Conf. **41**, 01011 (2013).

[40] M. Hofstetter, M. Schultze, M. Fieß, B. Dennhardt, A. Guggenmos *et al.*, Attosecond dispersion control by extreme ultraviolet multilayer mirrors, Opt. Express **19**, 1767 (2011).

[41] C. Bourassin-Bouchet, S. d. Rossi, J. Wang, E. Meltchakov, A. Giglia, N. Mahne, S. Nannarone, and F. Delmotte, Shaping of single-cycle sub-50-attosecond pulses with multilayer mirrors, New J. Phys. **14**, 023040 (2012).

[42] A. Guggenmos, Y. Cui, S. Heinrich, and U. Kleineberg, Attosecond pulse shaping by multilayer mirrors, Appl. Sci. **8**, 2503 (2018).

[43] P. K. Maroju, C. Grazioli, M. D. Fraia, M. Moioli, and G. Sansone, Attosecond pulse shaping using a seeded free-electron laser, Nature (London) **578**, 386 (2020).

[44] D. R. Austin and J. Biegert, Attosecond pulse shaping using partial phase matching, New J. Phys. **16**, 113011 (2014).

[45] R. Bartels, S. Backus, E. Zeek, L. Misoguti, G. Vdovin, I. P. Christov, M. M. Murnane, and H. C. Kapteyn, Shaped-pulse

optimization of coherent emission of high-harmonic soft x-rays, Nature (London) **406**, 164 (2000).

[46] S. Yamada, M. Noda, K. Nobusada, and K. Yabana, Time-dependent density functional theory for interaction of ultrashort light pulse with thin materials, Phys. Rev. B **98**, 245147 (2018).

[47] A. Yamada and K. Yabana, Multiscale time-dependent density functional theory for a unified description of ultrafast dynamics: Pulsed light, electron, and lattice motions in crystalline solids, Phys. Rev. B **99**, 245103 (2019).

[48] G. F. Bertsch, J.-I. Iwata, A. Rubio, and K. Yabana, Real-space, real-time method for the dielectric function, Phys. Rev. B **62**, 7998 (2000).

[49] SALMON official website, https://salmon-tddft.jp/.

[50] M. Noda, S. A. Sato, Y. Hirokawa, M. Uemoto, T. Takeuchi, S. Yamada, A. Yamada, Y. Shinohara, M. Yamaguchi, K. Iida, I. Floss, T. Otobe, K.-M. Lee, K. Ishimura, T. Boku, G. F. Bertsch, K. Nobusada, and K. Yabana, Salmon: Scalable *ab-initio* light-matter simulator for optics and nanoscience, Comput. Phys. Commun. **235**, 356 (2019).

[51] S. A. Sato and K. Yabana, Maxwell + TDDFT multi-scale simulation for laser-matter interactions, J. Adv. Simulat. Sci. Eng. **1**, 98 (2014).

[52] K. Yabana, T. Sugiyama, Y. Shinohara, T. Otobe, and G. F. Bertsch, Time-dependent density functional theory for strong electromagnetic fields in crystalline solids, Phys. Rev. B **85**, 045134 (2012).

[53] S. A. Sato, K. Yabana, Y. Shinohara, T. Otobe, and G. F. Bertsch, Numerical pump-probe experiments of laser-excited silicon in nonequilibrium phase, Phys. Rev. B **89**, 064304 (2014).

[54] C. Pemmaraju, F. Vila, J. Kas, S. Sato, J. Rehr, K. Yabana, and D. Prendergast, Velocity-gauge real-time TDDFT within a numerical atomic orbital basis set, Comput. Phys. Commun. **226**, 30 (2018).

[55] D. F. Edwards and H. Philipp, Cubic carbon (diamond), in *Handbook of Optical Constants of Solids* (Elsevier, Amsterdam, 1997), pp. 665–673.

[56] H. R. Philipp and E. A. Taft, Optical properties of diamond in the vacuum ultraviolet, Phys. Rev. **127**, 159 (1962).

[57] E. Goulielmakis, V. S. Yakovlev, A. L. Cavalieri, M. Uiberacker, V. Pervak, A. Apolonski, R. Kienberger, U. Kleineberg, and F. Krausz, Attosecond control and measurement: Lightwave electronics, Science **317**, 769 (2007).

[58] P. Földi, M. G. Benedict, and V. S. Yakovlev, The effect of dynamical Bloch oscillations on optical-field-induced current in a wide-gap dielectric, New J. Phys. **15**, 063019 (2013).

[59] V. S. Yakovlev, S. Y. Kruchinin, T. Paasch-Colberg, M. I. Stockman, and F. Krausz, Ultrafast Control of Strong-Field Electron Dynamics in Solids, *Ultrafast Dynamics Driven by Intense Light Pulses*, edited by M. Kitzler and S. Gräfe (Springer International Publishing, Switzerland, 2016), Vol. 86, pp. 295–315.

[60] X. Q. Zhang, F. Wang, Z. H. Liu, X. R. Feng, and S. N. Pang, Controlling energy transfer from intense ultrashort light pulse to crystals: A comparison study in attosecond and femtosecond regimes, Phys. Lett. A **384**, 126710 (2020).

[61] X. S. Kong, F. Wang, X. Q. Zhang, Z. H. Liu, and S. N. Pang, Controlling dielectric properties of CBN by an ultrashort double-pulse light, Phys. Lett. A **384**, 126125 (2020).

[62] X. Q. Zhang, F. Wang, L. Jiang, and Y. G. Yao, Manipulation of the dielectric properties of diamond by an ultrashort laser pulse, Phys. Rev. B **95**, 184301 (2017).

[63] Y. Shinohara, S. A. Sato, K. Yabana, J.-I. Iwata, T. Otobe, and G. F. Bertsch, Nonadiabatic generation of coherent phonons, J. Chem. Phys. **137**, 22A527 (2012).

[64] W.-C. Jiang and J. Burgdörfer, Dynamic interference as signature of atomic stabilization, Opt. Express **26**, 19921 (2018).

[65] W.-C. Jiang, S.-G. Chen, L.-Y. Peng, and J. Burgdörfer, Two-Electron Interference in Strong-Field Ionization of He by a Short Intense Extreme Ultraviolet Laser Pulse, Phys. Rev. Lett. **124**, 043203 (2020).

[66] K.-M. Lee, C. M. Kim, S. A. Sato, T. Otobe, Y. Shinohara, K. Yabana, and T. M. Jeong, First-principles simulation of the optical response of bulk and thin-film α-quartz irradiated with an ultrashort intense laser pulse, J. Appl. Phys. **115**, 053519 (2014).